

PFC/JA-82-16

Ion Cyclotron Resonance Heating Studies in
the Central Cell of the Phaedrus Tandem Mirror

B.D. McVey, R.A. Breun, S.N. Golovato
A.W. Molvik, D.L. Smatlak, D.K. Smith, and L. Yujiri

Department of Nuclear Engineering
University of Wisconsin
Madison, Wisconsin 53706

By acceptance of this article, the publisher and/or recipient acknowledges the U.S. Government's right to retain a nonexclusive, royalty-free license in and to any copyright covering this paper.

Ion Cyclotron Resonance Heating Studies in
The Central Cell of the Phaedrus Tandem Mirror

B. D. McVey,^(a) R. A. Breun, S. N. Golovato,
A. W. Molvik,^(b) D. L. Smatlak, D. K. Smith,^(a) and L. Yujiri

Department of Nuclear Engineering
University of Wisconsin
Madison, Wisconsin 53706

Abstract

Ion cyclotron resonance frequency heating experiments were performed in the central cell of the Phaedrus tandem mirror. The experiments were concerned with measuring and understanding the efficiency of RF power transfer to the plasma for the parameters and geometry of a tandem mirror central cell. Typically up to 200 kW were coupled to a $2 - 10 \times 10^{12} \text{cm}^{-3}$ plasma resulting in a ten fold increase in ion temperature to a maximum of 300 eV. Theoretical modelling of the experimental power balance suggests that loss mechanisms such as confinement loss, electron drag, and charge exchange do not account for all of the input power. Direct electron heating was observed in the experiment and could correct the power balance discrepancy. Finally, a discussion of the electron and ion heating mechanisms is presented.

I. Introduction

Ion cyclotron resonance frequency (ICRF) heating experiments have been performed in the central cell of the Phaedrus tandem mirror. The basic objective in these experiments was to understand the physics of the conversion of RF energy to plasma thermal energy for the particular geometry and plasma parameters of a tandem mirror central cell. Such an understanding is necessary to determine the utility of ICRF heating in the development of a tandem mirror reactor.

The use of ICRF heating in the central cell of a tandem mirror has a number of potential applications. Among these are a means of elevating the ion temperature during start-up which will reduce the trapping rate of cold central cell ions in the thermal barrier. A second application is to provide the energy input necessary to maintain a central cell plasma stream. The stream can be subsequently trapped in the end plugs, generating a target plasma for neutral beams.^{1,2} Finally, the β -stability boundaries of the tandem configuration can be tested by increasing the central cell beta with ICRF heating.^{3,4}

Ion cyclotron heating in magnetic mirrors has a long history dating back to the B-66 mirror experiments.⁵ These experiments were performed in a single axisymmetric mirror cell. Since then the mirror program has evolved to machines using single cell quadrupole minimum |B| mirrors and, subsequently, to tandem mirrors. The Phaedrus experiment is a classical tandem mirror with a solenoidal central cell bounded by quadrupole minimum

|B| end plugs. The experiment was specifically designed to test and develop RF heating techniques for the tandem mirror configuration. A number of separate heating experiments have been systematically performed on the machine. Fundamental⁶ and second harmonic⁷ ICRF heating experiments were performed in a single minimum |B| end plug. These experiments focussed on the trapping, heating, and density build up of a stream gun plasma in a single end plug. As will be reported here, ICRF heating experiments were performed in the central cell using stream gun injection and gas puffing to establish a target plasma. Finally, ICRF heating has been applied to both the central cell and end plugs generating an RF sustained plasma that persists approximately 10 msec beyond the turnoff of the stream guns.^{1,2}

Results of the RF heating experiments in the central cell of Phaedrus are reported as follows. Section 2 contains an overall description of the experiment, a listing of the diagnostics that were used, and a discussion of the RF antenna and matching circuit. Section 3 reports the experimental results of achievable ion energy density, efficiency of power transfer from the antenna to the plasma, and heating efficiency. These measurements were made for both a low density case (only stream gun injection), and a high density case (the addition of gas puffing). Other experimental results reported are: a comparison of ion heating for both an unshielded and Faraday shielded antenna, and a measurement of direct electron heating due to ICRH. In section IV, the results of a point code (power and particle balance) are presented. The modelling was found to be useful in understanding the observed heating efficiency, and would be useful in scaling the experimental results to other machines. Section 5 contains a discussion of the antenna-plasma coupling, and then ion heating rates for the estimated RF field levels in the plasma are calculated. Finally, section VI is a summary of the experimental results and theoretical modelling.

II. Description of the Experiment

We briefly describe the Phaedrus tandem mirror as is pertinent to the central cell ICRH experiments. A more detailed description of the machine configuration is contained in the references.^{8,9} The Phaedrus magnet set is shown in Fig. 1 with a scale indicating the size of the machine. Phaedrus is a classical tandem mirror that uses Ioffe coils and circular coils to generate minimum |B| end plugs which bound the solenoidal central cell. On each side of the central cell, two sets of recircularizing coils map the circular flux tube at the center of

the machine to orthogonal elliptical fans on the inside of each end plug. On the outside of each plug, recircularizers and solenoidal coils map the end plug elliptical fan to the circular aperture of the stream guns mounted on the end walls. Two Livermore-type hydrogenated titanium washer guns generate a target plasma for the ICRF heating experiments in the central cell by filling the tandem with plasma for pulse durations of 0.6 to 1.5 msec. Nearly all of the results presented in this paper are during stream gun operation. During stream gun operation, it is observed that line tying to the end walls enhances stability of the tandem⁴ and that thermal conduction to the end walls degrades the electron temperature.¹⁰ The stream guns provide a central cell target plasma of density $1 - 3 \times 10^{12} \text{cm}^{-3}$ with $T_e \sim 30 \text{ eV}$. Typically, the density in the end plug is comparable to the central cell density so that there is minimal electrostatic confinement of central cell ions.

Figure 2 is a plot of the magnetic field strength along the magnetic axis from the center of the machine to the inner mirror throats of the plugs. The central cell forms a deep magnetic well with the mirror ratio adjustable from 6 to 25. Near the bottom of the well, the flux tube is nearly circular with the quadrupole distortion becoming significant for $|B| > 1000 \text{G}$. During the ICRF heating experiment, no discernable physical effects such as resonant transport were attributed to the quadrupole distortion of the central cell flux tube. The position of the ICRH antenna, and the resonance field value are also indicated in Fig. 2.

The central cell diagnostics that were used are a monitor of the RF power input to the antenna, two diamagnetic loops, an interferometer, a number of Langmuir probes at a variety of azimuthal locations, and a small diamagnetic loop probe. The locations of the diamagnetic loops are indicated in Fig. 2. These loops provided a measure of the axial extent of the hot ion plasma; and, with a measurement of the radial extent of the plasma from Langmuir probes, the diamagnetic signals provide an absolute measurement of the energy content of the plasma and the RF power transfer to the plasma. The small diamagnetic loop probe provided a measure of the radial energy density profile. The plasma parameters of the end plugs were monitored with interferometers, diamagnetic loops, Thomson scattering in the east plug, and a charge exchange neutral analyzer in the west plug. End loss analyzers were located outside each end plug in the high field region and an end loss analyzer array was mounted on the west wall.

Figure 3 is a schematic illustration of the unshielded ICRF antenna that was used to

obtain nearly all of the results reported in this paper. The correct proportions of the central cell antenna and plasma size are indicated in the figure. The driven element of the antenna is a bare 7.5 cm wide, half-turn copper strap with radial feeders. The diameter of the half-turn is approximately 45 cm, and the radial feeders are approximately 45 cm in length. A limiter was provided to eliminate plasma bombardment and/or arcs in the direction of the magnetic field. The limiter consists of two 5 cm wide copper plates (only one shown in the figure) that shadow the driven element of the antenna. The limiter is positioned and supported by a single radial bar at the center of the half-turn loop. The vacuum breaks in the limiter are at the bottom and top of the antenna so that the gaps are well removed from the plasma discharge. The plasma is typically 20 cm in diameter with a peak density of $1 - 15 \times 10^{12} \text{cm}^{-3}$. During the experiment, the only observed arcing occurred after gun turn off when the central cell plasma was unstable and moved radially outward bombarding the antenna. A completely Faraday shielded half-turn antenna of nearly the same dimensions as in Fig. 3 was also constructed and tested. The Faraday shield consisted of 32 interleaving copper straps mounted on the vacuum tank that looped over the driven element of the antenna. Ridges on the copper straps eliminated line of sight to the plasma. In the next section, there is a comparison of the heating results obtained from the unshielded and Faraday shielded antennas.

The RF power circuit consisted of a tunable signal generator, a broad band ENI pre-amplifier, and final class C power tetrode amplifier stage. The operational frequency was 675 kHz corresponding to an ion cyclotron resonant field of 450 G. At this frequency, the antenna is essentially a lumped inductor with an inductance of $1.1 \mu \text{H}$. A 50,000 pF capacitor bank is used to parallel resonate the antenna providing a tank circuit that reasonably matches the output impedance of the tetrode. The power amplifier could deliver up to 200 kW depending upon the plasma loading of the antenna. Unloaded, the parallel antenna resistance was approximately 800Ω ; and with plasma loading, the resistance dropped to less than 200Ω , significantly below the output impedance of the tube (500Ω). An auto-transformer was inserted to improve the match, however the resonant frequency of the circuit was dependent on plasma loading, and detuning limited the power transfer. For the short pulses of the experiment where the loading resistance changes rapidly with time, direct connection of the antenna resonant tank to the output of the tube provided the maximum power transfer.

III. Experimental Results

The discussion of the experimental results will start with a brief description of a single shot. As previously stated, stream guns mounted on the vacuum tank end walls of the tandem provide a source of plasma. The plasma density rapidly builds in each end plug as the central cell fills more slowly. The curves of Fig. 4 display the density build up in the central cell for stream guns alone ($n_o = 0$), and for stream guns and various levels of gas puffing. The parameter n_o is the computed neutral density from pressure readings taken while filling the machine with neutral gas with the stream guns off. The dots and dashes in the figure represent averages over a number of shots of real data points with smooth curves drawn to fit the data. The plasma density peaks close to the turn off time of the stream guns. After gun turn-off, the central cell density drops quickly characterized by MHD activity due to the absence of plasma pressure in the end plugs or the elimination of line tying to the end walls.⁴ By increasing the plasma beta with ICRF heating, the plasma decay was observed to be more unstable resulting in more rapid loss. ICRF heating in the central cell alone was unable to sustain the plasma after the crow-bar of the stream gun. Referring again to Fig. 4, the plasma temperature at $t = 1.2$ msec was typically $T_e + T_i \sim 60eV$ for $n_o = 0$ and $T_e + T_i \sim 30eV$ for the highest density gas puff case where $n_o \sim 9 \times 10^{11} cm^{-3}$. The parametric dependence of the density build up with gas pressure was found to be a key element in creating a point model-particle and power balance code for analyzing the experiments (see section 4).

The primary heating results are contained in Figs. 5-9. The first three figures correspond to a high density gas puff case where $n_o \sim 7 \times 10^{11} cm^{-3}$, and the remaining two figures are with the plasma guns alone without gas puff. Figures 5-9 present heating and power transfer measurements as a function of the minimum magnetic field strength at the center of the central cell. Referring to Fig. 2, the axial variation of the magnetic field strength is shown for three points ($B_o(G) = 200, 450, 700$), of the abscissa in Figs. 5-9. The ion cyclotron resonant field is 450G and as the magnetic field strength is increased, the cyclotron resonance layer moves down the side of the magnetic well to an elongated cyclotron resonance layer at the bottom of the mirror, and finally out of the machine altogether.

As can be seen in Figs. 5 and 8, the highest ion temperatures are obtainable with the cyclotron resonance layer positioned at the bottom of the magnetic mirror. This result is in agreement with single particle heating theories (refer to Sec. 5) which state that the ion heat-

ing rate varies inversely with the gradient of the magnetic field evaluated at the resonance zone. Figure 5 is a plot of density and temperature measured at $t = 1.2$ msec (gun turn-off) with gas puffing. The density and temperature appear to rise linearly with magnetic field strength, peaking at the cyclotron resonance field, and then falling off. For a density of $1 \times 10^{13} \text{ cm}^{-3}$, a peak temperature of $T_e + T_i \sim 150 \text{ eV}$ was obtained. In this figure and Fig. 8, the temperature and density were computed from diamagnetic and interferometer signals assuming a plasma radius of 10 cm at 400G which was measured Langmuir probe scans. The plasma radius at other magnetic field strengths was computed assuming the stream guns always fill the same flux tube in the end plugs. This flux tube then maps to a central cell cross-sectional area that decreases linearly with magnetic field strength. In terms of the plasma beta, the highest temperatures in Fig. 5 translate to a peak beta of approximately 22%. The central cell beta considerably exceeded the end cell beta suggesting that line tying to the stream guns was providing MHD stability.

Figure 6 indicates the power input that was necessary to obtain the heating results of Fig. 5. The power subscripted "transfer" represents power transferred away from the antenna into the plasma. The power subscripted "absorbed" represents the power absorbed in the plasma as evidenced by the change in slope of the diamagnetic loop signal at turn-on or off of the RF pulse. In computing the power absorption, the plasma volume was derived from Langmuir probe data to obtain the plasma radius, and from two diamagnetic loop signals to estimate the axial extent of the plasma. The power transferred to the plasma remained relatively level at approximately 140 kW as the plasma parameters changed dramatically (refer to Fig. 5). The power absorbed by the plasma gently peaks near the resonance field at a value of 40 kW. This results in a peak heating efficiency of 28% with the efficiency dropping as the resonance zone is moved from the bottom of the mirror.

Figure 7 is a plot of the equivalent series plasma loading resistance (R_p). The antenna ohmic losses were $R_a = .03 \Omega$, and the ratio $R_p/(R_p + R_a)$ determines the wave launching or power coupling efficiency in the range of 70%. Note that for the experimental conditions reported in Fig. 7, 40 kW was absorbed by ohmic losses of the antenna in addition to the 140 kW transferred to the plasma. The ohmic power loss was not included in the calculated efficiency, since it is a characteristic of the low operational frequency and will be minimal for experiments at higher frequencies. From Figs. 6 and 7, it can be observed that saturation of the power output of the tetrode amplifier was a contributing factor to the limitation in

plasma heating. No catastrophic limit to the ion heating was observed during operation of the stream guns such as might be caused by a MHD beta limit. The loading resistance peaks at a magnetic field strength somewhat below the resonance field value. The peak in loading resistance corresponds to the resonance zone positioned in front of the antenna, an effect observed in fundamental ICRF heating experiments in the end plug.⁶ The plasma loading resistance only begins to decrease when the magnetic field is adjusted so that the cyclotron resonance layer is outside the machine. The loading resistance increased smoothly during the density build up of a shot. No loading spikes were observed as might be expected if the antenna coupled to propagating fast magnetosonic or ion cyclotron waves.

Figures 8 and 9 display temperature and power absorption for a low density plasma generated by the stream guns alone. Figure 8 is a plot of $T_e + T_i$ with and without RF heating. It is observed that the ion temperature peaks sharply at the cyclotron resonance field dropping rapidly on either side of resonance. For $T_e \sim 30\text{eV}$, the ion temperature during ICRF heating increases ten-fold. For the magnetic field scan in Fig. 8, the plasma density increases linearly with a value of $\sim 3 \times 10^{12}\text{cm}^{-3}$ at $B = 450\text{G}$. At the peak temperature of 250 eV, the plasma beta was $\sim 12\%$. Figure 9 displays the power transfer and power absorption curves corresponding to the temperature curve in the previous figure. The power transfer curve remains nearly constant up to the resonant field and drops abruptly. The plasma absorption peaks near 30 kW resulting in a heating efficiency of 40%. For fields such the $|B| > 500\text{G}$, the heating is non-resonant since the $\omega = \omega_{ci}$ layer is out of the machine. It is observed at 800G that approximately 20kW is transferred to the plasma with $\sim 4\text{kW}$ absorbed by the plasma. From Fig. 8 it is observed that $T_e + T_i \sim 80\text{eV}$ at this field value which increased from a value of $\sim 60\text{eV}$ without RF heating. Referring to Fig. 6, non-resonant heating at $B = 700\text{G}$ results in 120 kW transferred to the plasma with 15 kW absorbed. In this case, $T_e + T_i \sim 110\text{eV}$ as inferred from the diamagnetic loop data. From these results one can conclude that significant non-resonant heating and power transfer was observed. In addition, the non-resonant heating increases as the plasma density increases.

A heating comparison between the Faraday shielded and the unshielded antennas (described in the previous section) was made. The unshielded antenna had a heating efficiency of approximately a factor of two greater than the Faraday shielded antenna. The reason for the substantial difference in heating efficiencies is two fold. First, the Faraday shielded antenna has an unloaded Q of 60 compared to $Q = 160$ for the unshielded antenna.

For a plasma loading resistance of $80 \text{ m}\Omega$, the efficiency of power transfer for the unshielded antenna is $\sim 71\%$ and for the shielded antenna $\sim 50\%$. The ratio of the power transfer efficiencies suggests a ratio of 1.4 should be observed in the heating efficiencies. A second effect is that the close proximity of the Faraday shield to the antenna acts as a ground plane where a return current can flow. Detailed calculations of the magnitude of the return current for various geometries of Faraday shields has recently been reported.¹¹ Evidence of the return current is substantiated by the fact that the inductance of the antenna decreases when the Faraday shield is installed. An estimate of the decrease in inductance is approximately 15% implying the bucking current in the Faraday shield ground plane is 15% of the magnitude of the drive current. Since the power goes as the square of the current, the heating efficiency of the Faraday shielded antenna is decreased by a factor of 1.25 (corrected for constant voltage input) in addition to the factor of 1.4 described previously. These factors result in a ratio of 1.75 in the heating efficiencies for the two antennas which is reasonably close to the experimentally measured value of 2. It should be noted that the degradation in heating efficiency of the Faraday shielded antenna is in part due to the low operational frequency. A carefully designed Faraday shield¹¹, and a larger plasma loading resistance will minimize the degradation in heating efficiency due to the shield. It is noted in Fig. 13 that the plasma beta begins to saturate with RF level. This may be due to the finite gyro radius effects discussed previously.

During the central cell ICRF heating experiments, direct electron heating was observed as documented in Fig. 10. Thomson scattering measured the electron temperature in the east end plug during RF heating in the central cell. The Thomson scattering measurement was made at 1.4 ms, $200 \mu\text{s}$ after the crowbar of the stream guns. The time of RF turn-on and pulse length were varied to obtain the five cases presented in the figure. The top case is with no RF, and the electron temperature is measured to be 13.8eV. With ICRF heating throughout the gun pulse, the electron temperature is increased to 18.4eV and up to 20.9eV when the RF pulse is extended to the time of measurement. The short pulses of cases 4 and 5 indicate direct electron heating. In times short compared with the ion heating time such that electron drag on the ions does not heat the electrons, the electron temperature is seen to rise dramatically. The most effective heating of the electrons was obtained with a short RF pulse. It is interesting to compare cases 3 and 5 in Fig. 10. With the addition of ion drag heating of the electrons, case 3 should result in the largest electron temperature. This suggests that RF

heating throughout the stream gun pulse may modify the axial density profile such that the plug is thermally isolated from the central cell. We note that this effect occurs in a transient plasma that is decaying rapidly.

IV. Particle and Power Balance

In this section, the experimental results will be analyzed using a set of rate equations that determine the global particle and power balance for the central cell plasma. These equations are useful in determining the relative importance of power loss mechanisms such as charge exchange, axial confinement loss, and electron drag; and to determine whether these loss mechanisms can explain the observed heating efficiency.

The particle and power balance of the central cell ICRF heating experiments were modelled as described in the following. The stream gun was assumed to provide a specified central cell density, $n_g(t)$. The time evolution of the gun density was taken from the experimental observation of the central cell density build up without gas puffing (the lowest curve in Fig. 4). The temperature of the gun electrons was assumed to be a constant 30eV in accordance with Thomson scattering measurements in the east plug. The experiments with gas puff were modelled with the assumed $n_g(t)$, and the addition of a constant neutral pressure (n_o). The particle and power balance rate equations become:

$$\frac{d}{dt} n_e = \langle n_e n_o \sigma v \rangle_i + \langle n_g n_o \sigma v \rangle_i - \frac{n_e}{\tau_i} \quad (4.1)$$

$$n_i = n_e + n_g(t) \quad (4.2)$$

$$\frac{3}{2} \frac{dn_e T_e}{dt} = P_{ie} + P_{ge} - \frac{n_e (T_e + \Phi_e)}{\tau_i} \quad (4.3)$$

$$\frac{3}{2} \frac{dn_i T_i}{dt} = P_{RF} - P_{IE} - P_{IG} - \langle n_i T_i n_o \sigma v \rangle_{cx} - \frac{n_i T_i}{\tau_i^E} \quad (4.4)$$

The subscripts $g, i,$ and e represent gun electrons, ions, and electrons from the ionization of neutral gas, P_{RF} is the RF power density, the symbols P_{ij} represent the thermalization rates between various species averaged over Maxwellian distributions, and the notation $\langle \rangle$

represents ionization and charge exchange rates for a spatially averaged profile model. The confinement times are taken to be,

$$\tau_i = \tau_c + \tau_m \quad (4.5)$$

$$\tau_c = 1.3 \times 10^{-6} R L T_i^{-\frac{1}{2}} \quad (4.6)$$

$$\tau_m = 1 \times 10^6 \log(R) T_i^{\frac{3}{2}} n_i^{-1} \quad (4.7)$$

$$\tau_i^E = \left[\frac{\tau_c + \tau_m}{2\tau_c + \tau_m} \right] \tau_i \quad (4.8)$$

Where R is the mirror ratio, L is the effective length of the central cell, and Φ_c is the confining potential for electrons. The confinement time is taken to be a sum of collisional flow (τ_c) dominant at low ion temperatures, and an enhancement of confinement due to mirror trapping at higher ion temperatures (τ_m).¹²

The neutral model is illustrated in Fig. 11. The plasma is assumed to be a slab of uniform density of twice the thickness indicated in the figure immersed in a bath of molecular hydrogen. The random neutral flux of H_2 is burned out near the surface of the plasma with the ionized H_2^+ quickly dissociating generating the relatively low density of atomic H . The neutral density profiles were obtained using tabulated ionization and charge exchange cross sections which are averaged over a Maxwellian distribution.¹³ The neutral profile is then averaged over the slab cross section yielding the ionization rate coefficients $\langle n_o n_e \sigma v \rangle$ and $\langle n_o n_g \sigma v \rangle$ in Eq. 4.1, and the charge exchange rate coefficient in Eq. 4.4.

The rate equations were solved numerically, adjusting the input parameters $n_g(t)$, T_g , P_{RF} , and n_o to closely model the experimentally measured parameters, n_i and $T_i + T_e$. For stream gun injection and various levels of gas puffing, Fig. 12 displays code results modelling the experimentally measured density build up of Fig. 4. The density build up can be closely modelled for values of the neutral density that are approximately the experimentally measured pressures. This implies that the particle confinement times and ionization rates are reasonably modelled in the point code.

The ICRF heating experimental results of Figs. 5-9 can be modelled with the addition of RF heating ($P_{RF} \neq 0$) in the point code. Table 4.1 summarizes results for the gas puff case for $n_0 = 7 \times 10^{11}$ and $1 \times 10^{12} \text{cm}^{-3}$. These results are to be compared with the measured experimental parameters of Figs. 5-7 which were obtained with 140 kW of RF input power. For input powers in the range of 40 to 50 kW, the point code yields parameters close to the experimentally measured values. Energy confinement loss accounted for approximately 50% of the input power, and the remainder is divided between electron drag and charge exchange loss. Referring to Fig. 7, the input power in the calculation reasonably matches the power absorbed as inferred from the diamagnetic signal, however, there is a large discrepancy between the point code results and the power transferred from the antenna. Variational studies with the point code over the range of uncertainty of input parameters (such as gun electron temperature) suggest that at most only 50% of the input power can be accounted for by the loss mechanisms in the code. A similar result occurs when modelling the low density heating case of Figs. 8 and 9. The experimental ion temperature of approximately 200eV was obtained with $P_{rf} = 13$ kW in the point code, while in the experiment, 50-60 kW of input power was required.

One explanation for the discrepancy in the power balance is that the ICRF directly heats the electrons as documented in Fig. 10. During stream gun injection, the electrons are thermally tied to the end walls acting as an energy sink. An estimate of the power that could be coupled to the central cell electrons can be obtained from the formula of Cohn, et. al.,¹⁴ which relates the central cell electron temperature (T_e) to that of a passing stream (T_g).

$$\frac{3}{2} \frac{dn_e T_e}{dt} = -\left(\frac{2IR}{G} + 1\right)(nT)_v \quad (4.9)$$

where

$$(nT)_v = 8.9 \times 10^{-24} \frac{n_e n_g}{R} \left[\ln \left(\frac{n_e}{n_g} \sqrt{\frac{T_g}{T_e}} \right) \right]^{-1} \times \left(\frac{T_e}{T_g} \right)^{\frac{1}{2}} \frac{(T_e - T_g)}{T_e^{\frac{3}{2}}}$$

For Phaedrus parameters, the first factor in Eq. 4.9 is 6.5 assuming a central potential to electron temperature ratio of one. Then for $T_e = 40$, $T_g = 30 \text{eV}$, $n_e = 4 \times 10^{12}$, and $n_g = 1.3 \times 10^{12}$, Eq. 4.9 yields a required power density of 1.25 W/cm³. This corresponds to a total input power of 80 kW, and it is clear that the central cell electrons are thermally tied to the external gun plasma. Thus, direct power loss to the electrons may account for the power balance discrepancy in the point code.

V. Antenna Coupling and Heating Rates

The coupling of the antenna fields to the plasma are discussed in this section. In addition, heating rate calculations are made incorporating ICRF and mirror physics not contained in the point model of the previous section.

At the operational frequency of 675 KHz, the free space wavelength is approximately 450 m; and to an extremely good approximation, magnetostatics can be used to obtain the applied RF magnetic field. Associated with the time varying magnetic field is an inductive electric field that can be computed using the vector potential. The antenna of Fig. 3 is modelled as a line source with image current as diagrammed in Fig. 13. For a line source of current, the applied vacuum fields can be readily calculated in the volume occupied by the plasma.

$$E_y^v = \frac{i\omega\mu_0 I}{4\pi} \ln \left[\frac{(x - x_1 - 2x_2)^2 + z^2}{(x - x_1)^2 + z^2} \right] \quad (5.1)$$

$$B_z^v \sim \frac{\mu_0 I}{2\pi} \frac{(x_1 - x)}{(x_1 - x)^2 + z^2} \quad (5.2)$$

$$B_x^v \sim \frac{\mu_0 I}{2\pi} \frac{z}{(x_1 - x)^2 + z^2} \quad (5.3)$$

In the above equations, the image is retained for the electric field to exclude a logarithmic singularity. The calculation of the applied vacuum electric field does not consider charge build up on the antenna and is only valid in the interior of the plasma where electrostatic fields are shielded. For a circulating current in the antenna of 2000 A (typical in the experiment), the applied left-hand polarized electric field is $|E_+| = 15$ V/cm at the position $x = z = 0$ in Fig. 13. As will be subsequently discussed, this value of E_+ is much larger than necessary to explain the observed heating. It is thus concluded that the plasma significantly shields the applied field, and this conclusion is verified by numerical calculations.

A computer code has been written that calculates the linear self-consistent plasma fields, the loading resistance, and the power absorption for the antenna and plasma geometry of Fig. 17.^{15,16} The following assumptions were made for the equilibrium parameters of the plasma. The plasma is confined by a uniform magnetic field, and the plasma density is uniform in z and r and abruptly drops to zero at a radius $r = a$. The plasma is assumed

to be bi-Maxwellian with temperatures T_{\perp} and T_{\parallel} , however, finite gyro radius corrections are neglected. For these conditions, two modes propagate in the plasma defined by the perpendicular wave numbers k_{\perp}^f and k_{\perp}^s . For $k_o^2 S \neq k_z^2$,

$$(k_{\perp}^f)^2 \approx \frac{(k_o^2 L - k_z^2)(k_o^2 R - k_z^2)}{(k_o^2 S - k_z^2)} \quad (5.4)$$

$$(k_{\perp}^s)^2 \approx \frac{P}{S}(k_o^2 S - k_z^2) \quad (5.5)$$

where k_o is the free space wave number, k_z is the axial wave number determined by the Fourier spectrum of the antenna, and S, R, L and P are the equivalent dielectric elements using the notation of Stix¹⁷ and are defined in reference 16. Equation 5.4 determines the propagation characteristics of the long wavelength fast magnetosonic mode and the ion cyclotron wave, and Eq. 5.5 is for the (short wavelength) electrostatic ion cyclotron wave or kinetic Alfvén wave. Both of these modes contribute to the self-consistent electric field calculations for the antenna geometry of Fig. 13.

Figure 14 plots results of the variation of the $|E_{+}|$ field computed along the chord ($z = 0, -a \lesssim x \lesssim a$), for the various plasma densities indicated and for the plasma parameters listed in the caption. It is observed that the plasma shields the applied field by a factor of ten, and the amount of shielding is sensitive to plasma density. The shielding can be simply explained as the polarization characteristics of an evanescent fast magnetosonic wave which is dominantly right hand polarized at a frequency close to the cyclotron frequency. The plasma density and radius are such that the RF drive frequency is below the cut off frequency of a propagating fast magnetosonic mode. The monotonic increase of $|E_{+}|$ with reduced density and in a direction toward the antenna, suggests that surface heating should be significant in the experimentally measured ion heating.

Figure 15 is a plot of the computed loading resistance as a function of plasma density. It is found that this loading resistance is primarily due to electron heating even though $\omega = \omega_{ci}$. We have concluded that the theoretical model of Fig. 17, accurately computes plasma loading for propagating modes alone. Plasma loading due to heating of trapped ions bouncing in and out of the evanescent near fields of the antenna is not properly modelled. The loading resistance of $\sim .015\Omega$ corresponds to excitation and electron Landau damping of the slow mode defined by Eq. 5.5. A simple picture is the following. The inductive fields

of the antenna couple to the long wavelength fast magnetosonic mode which is evanescent. The reactive plasma currents of the fast wave have an electrostatic component ($\nabla \cdot E' \neq 0$), and can couple to short wave length electrostatic modes at the boundary or in a density gradient. The loading resistance of $\sim .015\Omega$ compares favorably to the observed non-resonant loading in Figs. 7 and 9. However, the decrease of the plasma loading resistance with density contrasts the experimental results. We note that excitation of short wavelength modes by inductive coils has been observed in an ICRF heating experiment,¹⁸ and is believed to be responsible for the efficient second harmonic heating in the Phaedrus end plug.⁷

In the remainder of this section, we calculate heating rates for ions interacting with the evanescent $|E_+|$ fields of the antenna. A stochastic ion heating model is assumed. An ion interacts with the wave in the resonance zone gaining or losing energy dependent upon the phase of the electric field vector relative to the velocity vector of the ion. A simple power absorption formula can be derived by assuming that ions free-stream through a periodic structure of resonance zones separated by a distance L ,¹⁹

$$P_{RF}(\omega/cm^3) = 2\pi qn \frac{|E_+(v/m)|^2}{LB'(res)} \quad (5.6)$$

where n is the plasma density, and $B'(res)$ is the gradient in the magnetic field evaluated at the resonance zone. For $n = 10^{13}cm^{-3}$, $LB'(res) = .032T$, and $P_{RF} = 1.2\omega cm^{-3}$, we calculate $|E_+| = .62Vcm^{-1}$. This value is high by about a factor of two compared with the value of the electric field predicted in Fig. 14, however it does indeed verify the shielding properties of the plasma were observed in the experiment.

The heating model of Eq. 5.6 shows an inverse dependence of the power absorption with $B'(res)$. This effect is qualitatively verified from the results of Figs. 5-9 where the greatest heating was obtained with the resonance zone positioned so as to minimize $B'(res)$. The heating model also shows a linear dependence with density which contradicts the experimental results. Those results show that the power absorption had a linear increase with density, however it is not directly proportional to density. The experimental results would be compatible with Eq. 5.6, if one assumes $|E_+|$ decreases by a factor of 1.4 as the density increases from 1 to $5 \times 10^{12}cm^{-3}$. This dependence is in qualitative agreement with the theoretical results of Fig. 14.

More realistic and accurate heating rate calculations can be made by using the Monte

Carlo method to follow an ensemble of test ions in a magnetic mirror geometry.²⁰ In such a calculation, the ions cross the resonance zone and obtain a kick in perpendicular energy of the following form for atomic hydrogen.

$$\Delta E_{\perp}(eV) = \Delta E_{\perp}^c + \Delta E_{\perp}^s \quad (5.7)$$

$$\Delta E_{\perp}^c(eV) = 4.8 \times 10^{11} E_{\perp}^2 (v/cm) T_r^2 \quad (5.8)$$

$$\Delta E_{\perp}^s(eV) = 1.38 \times 10^6 E_{\perp}^{\frac{1}{2}}(eV) E_{\perp} (v/cm) T_r \cos \phi \quad (5.9)$$

In the above equations, ΔE_{\perp}^c represents a coherent or positive definite upward acceleration by the RF fields, and E_{\perp}^s represents upward or downward diffusive step-size dependent upon the random phase (ϕ) between the RF field and the velocity vector of the particle. The interaction time of an ion with the RF field in the cyclotron resonance layer is given by,

$$T_r = \frac{2\pi}{(2|c_2|)^{\frac{1}{2}}} A_i \left[\frac{-c_1}{(3|c_2|)^{\frac{1}{2}}} \right] \quad (5.10)$$

$$c_1 = \frac{1}{2} \omega'_c v_r \quad (5.11)$$

$$c_2 = -\frac{1}{6} (\omega'_c a_r + \omega''_c v_r^2) \quad (5.12)$$

where v_r and a_r are the parallel velocity and acceleration of the particle at the resonance zone, ω'_c and ω''_c are the first and second spatial gradients of the ion cyclotron frequency evaluated at the resonance zone, and A_i is the Airy function.

The interaction time has two limiting forms of interest; (1) an ion turning exactly at the resonance zone, and (2) an ion streaming through the resonance zone. The coherent acceleration per pass for these two cases is given by,

$$(1) \quad \Delta E_{\perp}^c(eV) = 5800 \cdot |E_{\perp}|^2 (B')^{-\frac{1}{2}} (E_{\perp})^{-\frac{1}{2}} \quad (5.13)$$

$$(2) \quad \Delta E_{\perp}^c(eV) = 320 \cdot |E_{\perp}|^2 (B')^{-1} (E_{\parallel})^{-\frac{1}{2}} \quad (5.14)$$

Note that one can derive Eq. 5.6 from 5.14 by summing over a density of ions with an average velocity (E_{\parallel}^{\dagger}). Table 5.1 lists typical coherent step-size for a variety of ion energies, normalized to $E_{+} = 1Vcm^{-1}$ and $B' = 4Gcm^{-1}$. It is observed that the heating per pass of low energy ions is very large for ions that turn near the resonance zone. The step-size of the ion heating suggests strong radial expansion of the plasma column near the cyclotron resonance layer, and as a result, finite gyro radius effects may limit the heating.

Table 5.2 summarizes results of a Monte Carlo code which follows 500 test ions to a steady-state equilibrium with 30 eV electrons, and for an ion source with an initial energy of 5 eV. The code assumes the ambipolar potential is zero, and only power loss due to electron drag and scattering into the loss cone are reflected in the results of Table 2. The low density case was run to simulate the experimental results of Figs. 8 and 9, and the high density runs, the experimental results of Figs. 5-7 both for $B = 400G$. For various levels of the $|E_{+}|$ field component, the RF power density, the equilibrium average ion energy, average confinement time, and average loss energy are tabulated. It is observed in the low density case, that a power input of approximately 10 kW results in an ion temperature of 250 eV. This agrees with the point code modelling, however contrasts the required 55 kW in the experiment to obtain a similar temperature. In Table 5.2, τ' is the confinement time computed from Eq. 4.5, and it is found to be larger than the confinement time from the Monte Carlo code. The RF diffusive term in Eq. 5.7 results in the decrease in the particle confinement time. The electric field necessary to model the experiment is approximately $.8Vcm^{-1}$ which is in fair agreement with the field predictions of Fig. 14.

The high density Monte Carlo run requires 80 kW of power input for best agreement with the experimentally observed temperature of 120 eV for 140 kW of power input. Again there is a discrepancy of 60 kW, some of which may be accounted for by charge exchange losses or direct electron heating. For the high density case, the confinement time of Eq. 4.5 is in close agreement with the Monte Carlo code results. However, the required electric field of $1.25Vcm^{-1}$ is much larger than predicted by the antenna calculation of Fig. 18. One possible explanation is that surface heating is more important in the high density case. The E_{+} field is shielded from the center but has a large value near the surface of the plasma where the density is lower. Ions with large gyro radii could sample the higher fields at the surface.

VI. Summary and Discussion of Results

Data analysis and modelling of the ICRF heating experiments in the central cell of Phaedrus have focussed on understanding the efficiency of RF power transfer to the plasma. Two experimental cases were analyzed in detail. First, ICRF heating was applied to a high density plasma ($n \sim 10^{13} \text{cm}^{-3}$) formed by stream gun injection and gas puffing. Application of up to 150 kW to the plasma resulted in an increase of ion temperature from approximately 10 to 120 eV with a peak heating efficiency of 28%. ICRF heating of a low density plasma ($2.3 \times 10^{12} \text{cm}^{-3}$), with 50 kW coupled to the plasma, resulted in peak ion temperatures of 250 eV and a heating efficiency of 40%. The heating efficiency in both cases was maximum with the cyclotron resonance layer located at the bottom of the magnetic mirror. The plasma absorption was found to increase with density although it was not directly proportional to density. Significant nonresonant absorption was observed by removing the cyclotron resonance layer from the plasma. For the experimental conditions, an unshielded antenna was found to be more efficient than a Faraday shielded antenna. Finally, direct electron heating was observed in the experiment.

Theoretical modelling of the experimental results was divided into two areas. First, a point code particle and power balance analysis was made. For the high density case, approximately 50 kW of the 140 kW was accounted for with the losses divided among charge exchange, confinement loss, and electron drag. For the low density case, only 10 out of 55 kW could be attributed to those loss mechanisms. Direct electron heating may account for some or maybe all of the missing power loss. During stream gun injection, the electrons will act as an energy sink since their temperature is limited by thermal conduction to the walls. More detailed heating rate and antenna coupling calculations were made. The antenna calculation showed direct excitation of an electrostatic mode that heated the electron via Landau damping. The modelling further demonstrated shielding of the left hand circularly polarized electric field component. The polarization shielding was clearly demonstrated in the experiment, and the absolute value of electric fields estimated from heating rate calculations were in qualitative agreement with the antenna calculations.

We acknowledge R. S. Post for initiating this experiment, F. H. Coensgen and T. C. Simonen for making it possible for the loan of the ICRH transmitter, and Paul Nonn for integrating the transmitter into the Phaedrus experiment. This work was performed for U. S.

DOE Contract DE-AC02-78ET-51015 and DE-AC02-78ET-51013.15.

- (a) Permanent address: Plasma Fusion Center, Massachusetts Institute of Technology, Cambridge, Massachusetts 02139.
- (b) Permanent address: Lawrence Livermore National Laboratory, Livermore, California 94550.

References

1. Breun, R., Golovato, S.N., Yujiri, L., McVey, B., Molvik, A., Smatlak, D., Post, R.S., Smith, D.K., Hershkowitz, N. "Experiments in a Tandem Mirror Sustained and Heated Solely by RF," *Phys. Rev. Lett.*, 47 (1981) 1833.
2. Breun, R. "Proceedings of the Workshop, Ambipolar Potential Formation and Control in Bumpy Tori and Mirrors," CONF-810511, Oak Ridge, Tenn. (1981) 109.
3. Molvik, A. W., Breun, R.A., Golovato, S.N., Hershkowitz, N., McVey, B., Smatlak, D., Yujiri, L. Lawrence Livermore National Laboratory Report UCRL-86863, submitted to *Phys. Rev. Lett.* (1981).
4. Molvik, A. *Bull. Am. Phys. Soc.*, 26 (1981) 1021.
5. Hooke, W. M., Tenney, F. H., Brennan, M. H., Hill, H. M., Stix, T. H., *Phys. Fluids*, 4 (1961) 1131.
6. Smith, D. K. "Fundamental Resonance Ion Cyclotron Heating in the Phaedrus Plug Mirrors," Ph.D. Thesis, University of Wisconsin (1980).
7. Golovato, S. N., McVey, B. D., Scharer, J. E., Breun, R. A., Smith, D. K., Yugo, J., and Yujiri, L. "Plasma Heating at Twice the Ion Cyclotron Frequency in a Quadrupole Minimum- $|B|$ Mirror," submitted to *Nucl. Fusion* (1981).
8. Breun, R., Conrad, J. R., Golovato, S. N., Kesner, J., Post, R. S., et. al. "Initial Results from the Tandem Mirror Phaedrus," Plasma Physics and Controlled Nuclear Fusion Research (*Proc. 8th Int. Conf.*, Brussels, 1980) *IAEA, VIF*, Vienna (1981) 105.
9. Post, R. S., et. al. "Investigation of RF Heating for Tandem Mirror Experiments and Reactors," Project Proposal, University of Wisconsin (1977).
10. Smatlak, D. L., Breun, R. A., Gamage, D., Golovato, S. N., Smith, D. K., Yujiri, L. *Bull. Am. Phys. Soc.*, 25 (1980) 860.
11. Faulconer, D. W. *Bull. Am. Phys. Soc.*, 26 (1981) 897.
12. Rognlien, T. D., Cutler, T. A. *Nucl. Fusion*, 20 (1980) 1003.
13. Freeman, R. L., Jones, E. M. "Atomic Collision Processes in Plasma Physics Experiments," Culham Laboratory, CLM-R, 137.
14. Cohen, R.H., Bernstein, E.B., Dorning, J.L., Rowlands, G., *Nucl. Fusion*, 20 (1980) 1421.

15. McVey, B. D., Breun, R. A., Golovato, S. N., Post, R. S., Scharer, J. E., Smith, D. K. *Bull. Am. Phys. Soc.*, 25 (1980) 860.
16. McVey, B. D. "Excitation Theory of the Inductive Drive," Task II Report-2740, TRW.
17. Stix, T. H. *The Theory of Plasma Waves*, McGraw-Hill, New York (1962).
18. Clark, R. W., Swanson, D. G., Korn, P., Sandel, F., Robertson, S., Wharton, C. B. *Phys. Fluids*, 17 (1974) 1322.
19. Eldridge, O. *Phys. Fluids*, 15 (1972) 676.
20. Rognlien, T. D., Matsuda, Y. *Nucl. Fusion*, 21 (1980) 345.

Point Code Results

$n_o(cm^{-3})$	$t(ms)$	$P(kW)$	$n_i(cm^{-3})$	$T_i(eV)$	$P_{drag}(kW)$	$P_{cz}(kW)$	$P_{conf}(kW)$
7×10^{11}	.9	38	5.2×10^{12}	116	6.7	5.5	14.1
	1.2		$7. \times 10^{12}$	103	10.0	5.1	21.1
1×10^{12}	.9	52	6.7×10^{12}	110	10.8	8.1	21.3
	1.2		8.6×10^{12}	100	14.9	7.5	28.6
5×10^{10}	.9	13	1.5×10^{12}	210	1.0	.6	1.1
	1.2		2.6×10^{12}	190	2.6	.6	3.2

Table 4.1

ICRF Heating Step-Size

$E_{\perp}(eV)$	$E_{\parallel}(eV)$	$\Delta E_{\perp}^c(eV)$		$\rho_i(cm)$
		(1)	(2)	
10	10	250	25	1
50	50	85	12	2.3
100	100	54	8	3.2
200	200	34	6	4.5
400	400	21	4	6.4

Table 5.1

Monte Carlo Code Results

$n(\text{cm}^{-3})$	$ E_+(v/cm) $	$P(\text{kW})$	$T_i(\text{eV})$	$\tau(\text{ms})$	$\tau'(\text{ms})$	$E_e(\text{eV})$
3×10^{12}	.75	7.7	150	1	1.1	90
3	1	14.7	360	1.7	3.2	120
3	1.2	21.1	600	2	6.8	130
1×10^{13}	1	40	70	.45	.51	90
1	1.25	77	120	.55	.515	120
1	1.5	96	200	.7	.63	150

Table 5.2

Figure Captions

- Fig. 1 - The Phaedrus magnet set.
- Fig. 2 - Axial $|B|$ profile of the central cell of Phaedrus for three values of $B_{min} = 200, 450, 700$. The symbol "D" indicates the position of diamagnetic loops, and the position of the ICRH antenna is shown along with the $|B|$ value for cyclotron resonance.
- Fig. 3 - The unshielded central cell antenna showing the driven element and half of the limiter. Dimensions are in centimeters.
- Fig. 4 - Experimental measurement of the central cell density build up for various levels of neutral density.
- Fig. 5 - Peak density and perpendicular temperature as a function of the magnetic field strength at the center of the machine. A high density gas puff case.
- Fig. 6 - Heating efficiency as a function of the magnetic field strength at the center of the machine. A high density gas puff case.
- Fig. 7 - Plasma loading resistance as a function of the magnetic field strength at the center of the machine. A high density gas puff case.
- Fig. 8 - Peak perpendicular temperature as a function of the magnetic field strength at the center of the machine. \circ - no RF heating, \cdot with RF heating. A low density case.
- Fig. 9 - Heating efficiency as a function of the magnetic field strength at the center of the machine. \circ - no RF heating, \cdot with RF heating. A low density case.
- Fig. 10- Electron temperature measurement in the east plug during ICRF heating in the central cell.
- Fig. 11- Plasma slab model for calculation of the neutral density profile. The slab is symmetrical about the right hand ordinate.
- Fig. 12- Theoretical modelling of the density build up using the rate equations of section 4.
- Fig. 13- Geometry for RF field calculations modelling the experimental geometry of Fig. 3.
- Fig. 14- Radial profiles of the $|E_{+}|$ field for the antenna geometry of Fig. 17. $B = 450G, T_e = 30eV, T_{\perp i} = 150eV, T_{\parallel i} = 75eV$, hydrogen plasma, $I = 2000A, x_1 = 22cm, x_2 = 48cm, \omega = \omega_{ci}$.

Fig. 15 Plasma loading resistance as a function of plasma density. Parameters are the same as Fig. 18.

Fig. 1

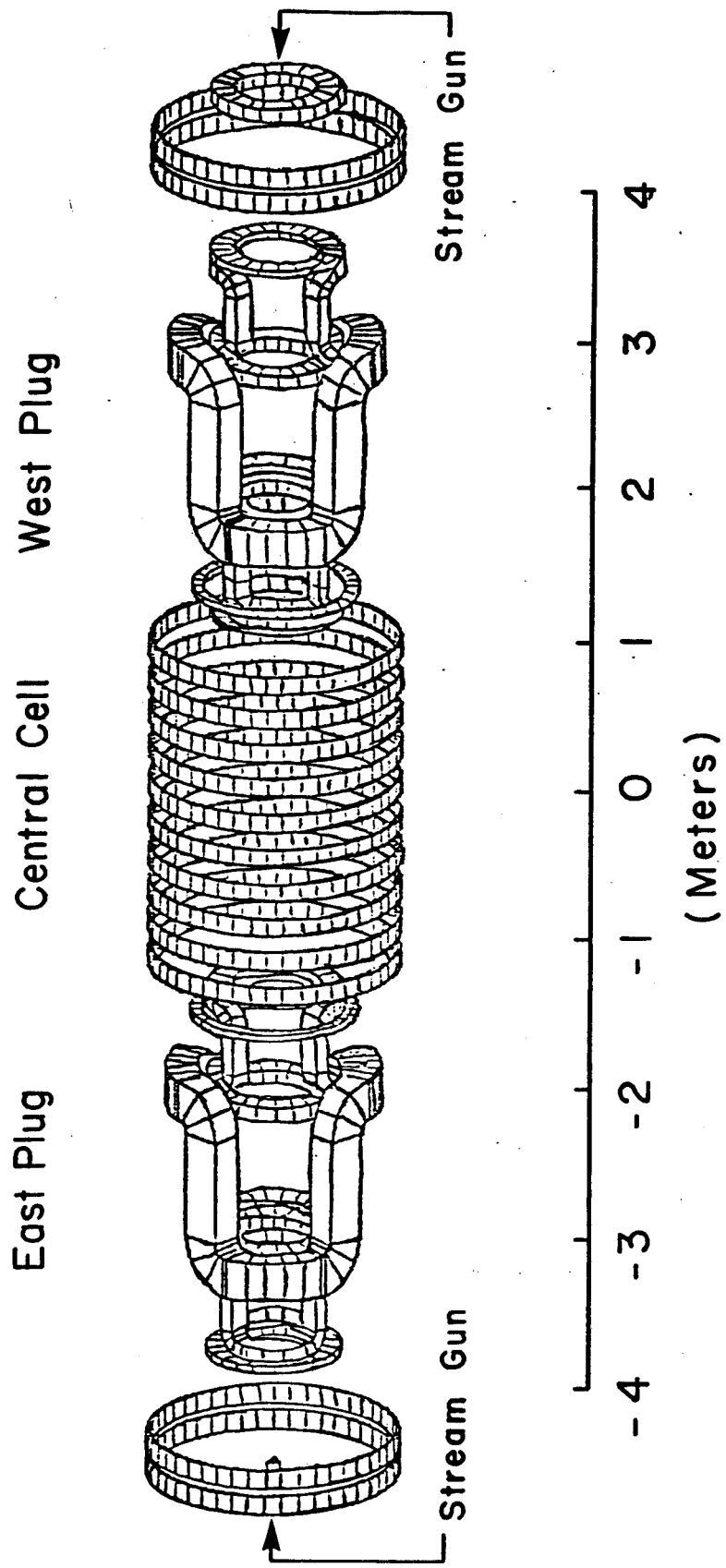


Fig. 2

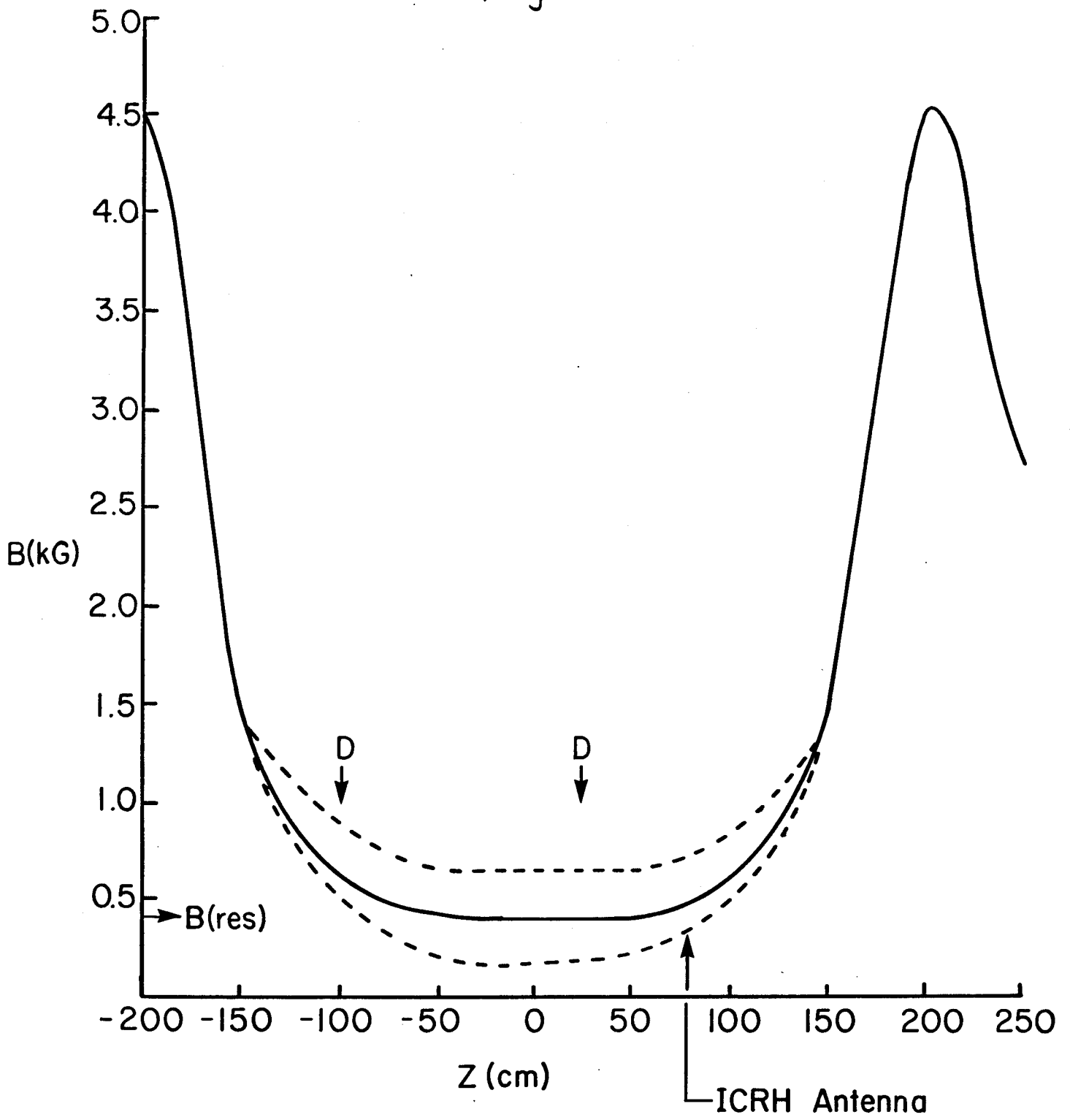


Fig. 3

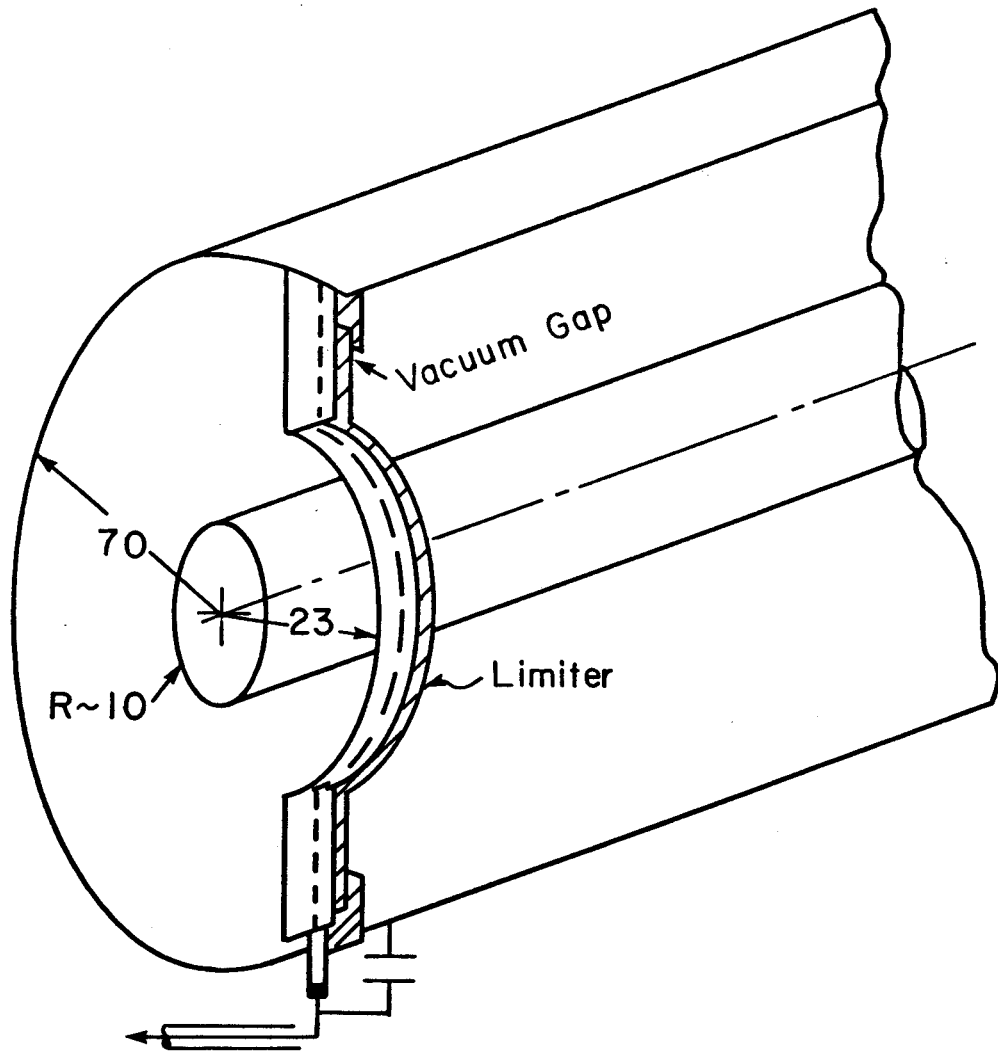


Fig. 4

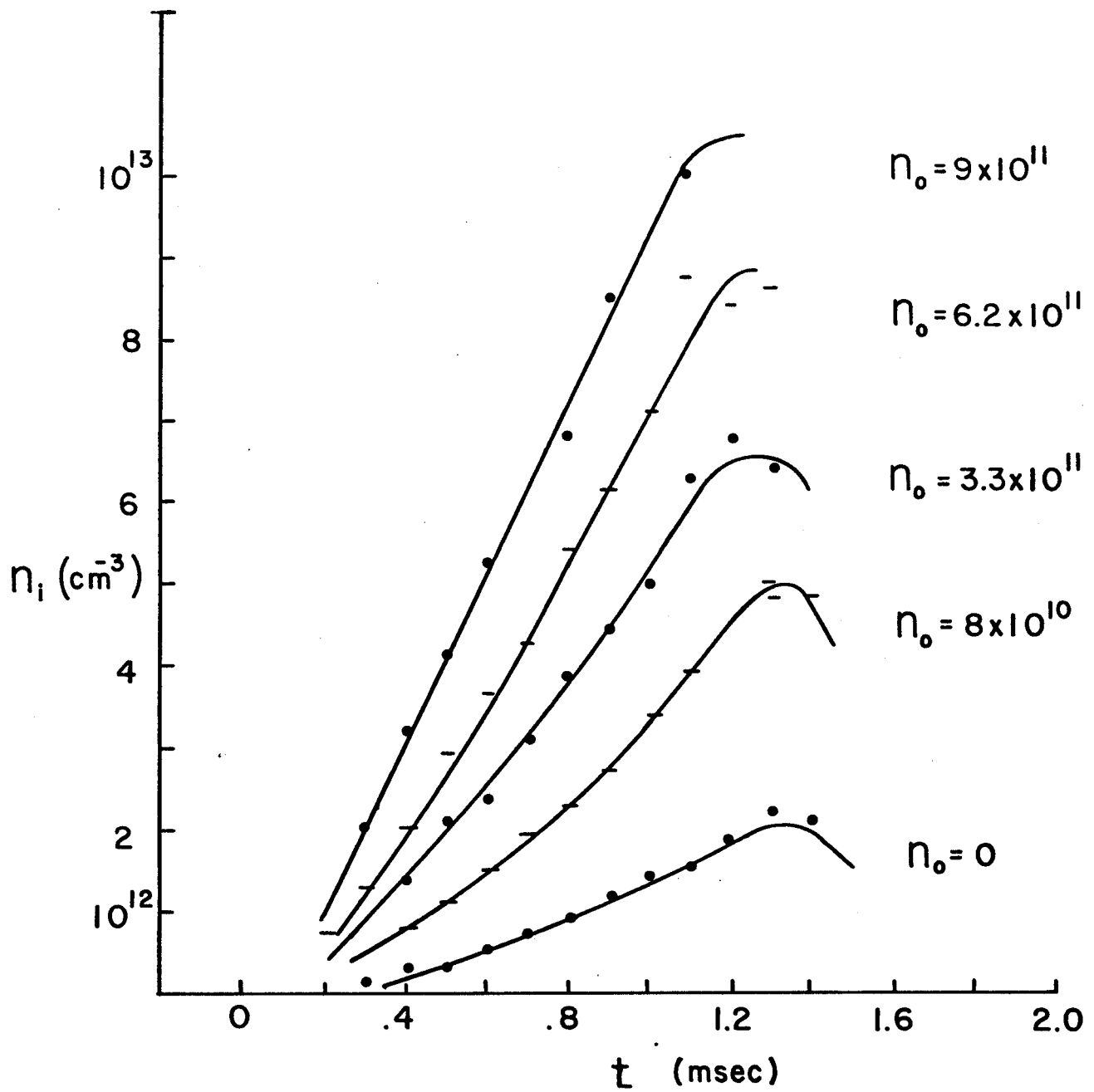


Fig 5

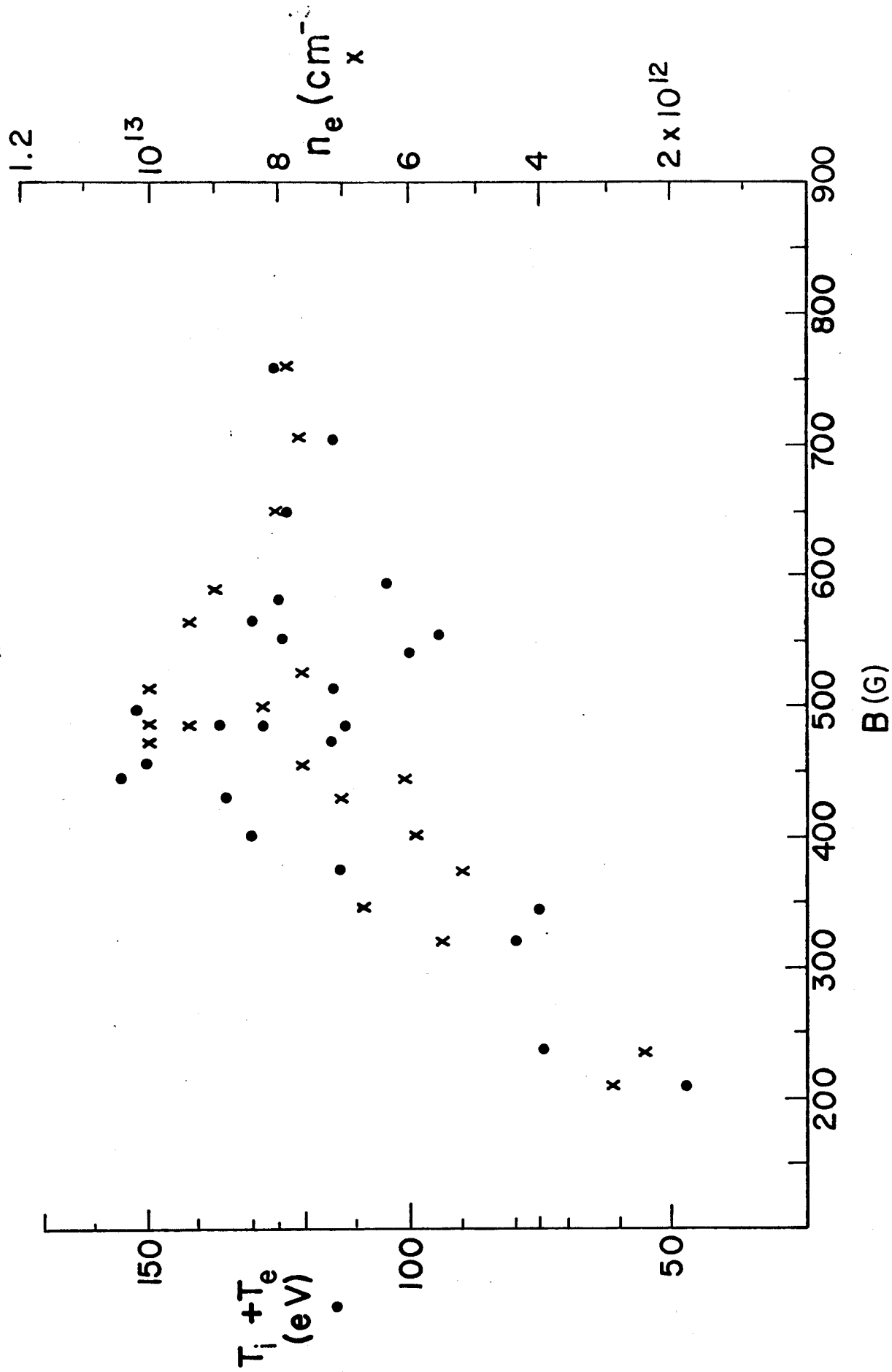


Fig. 6

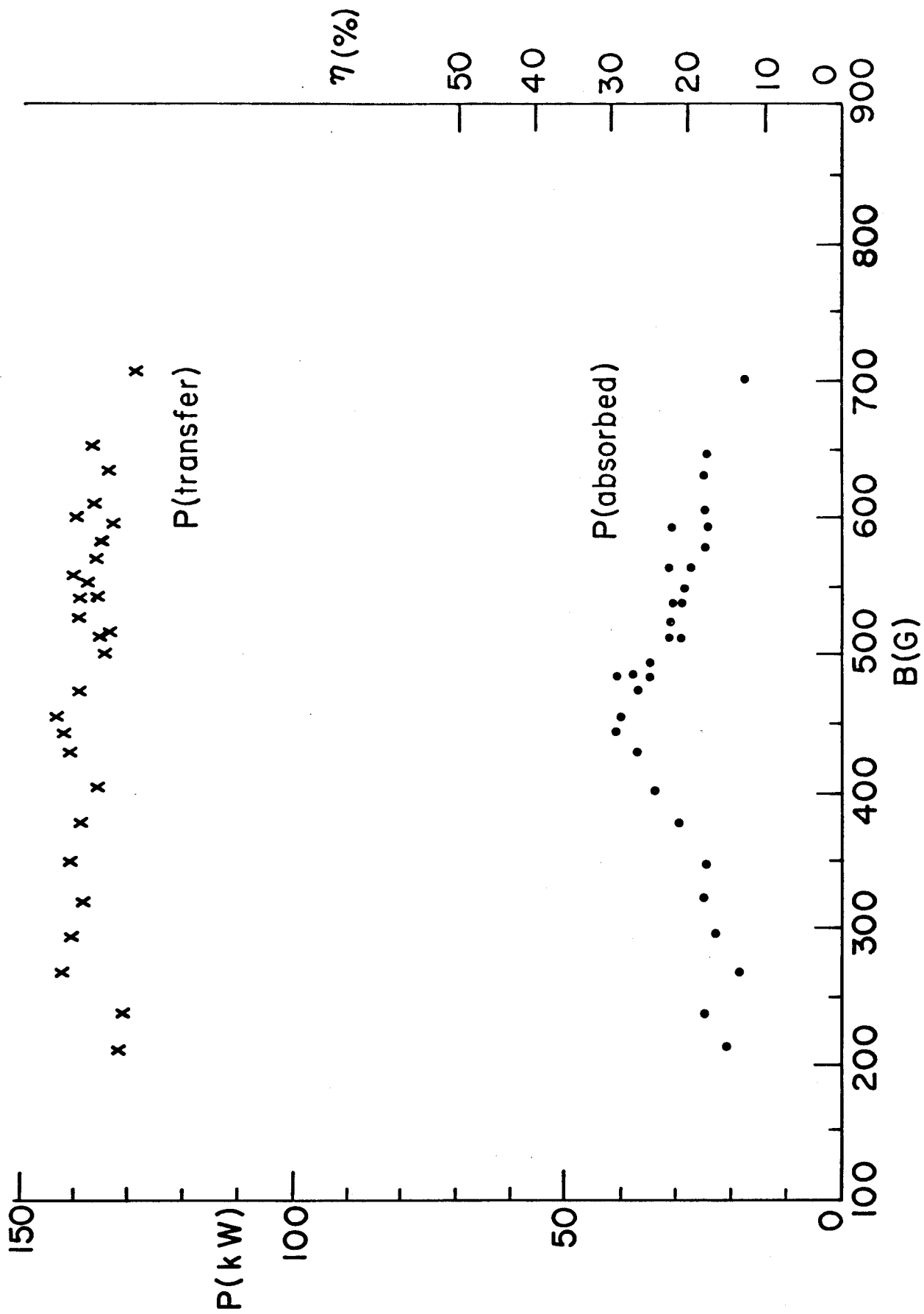


Fig. 7

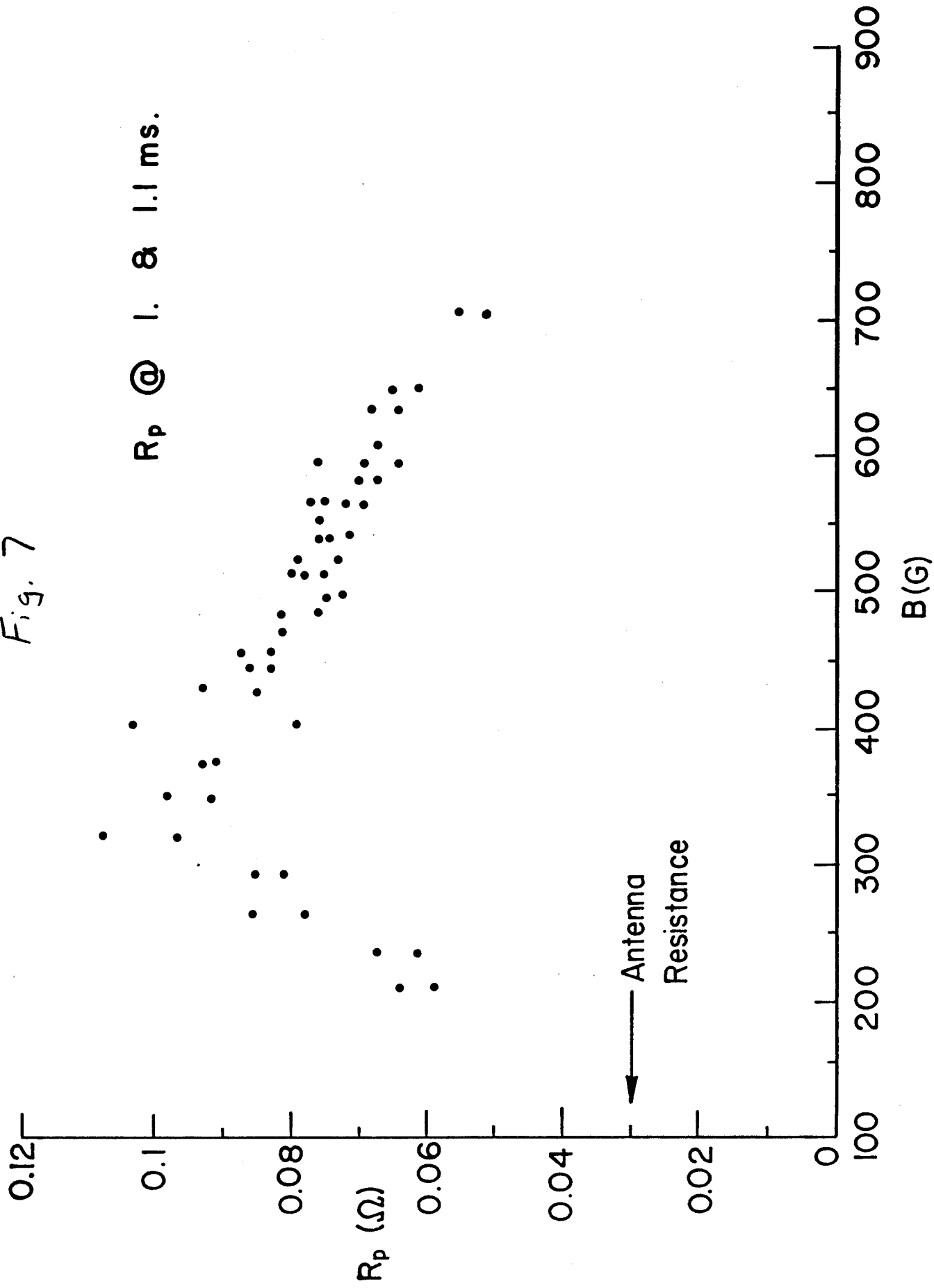


Fig. 8

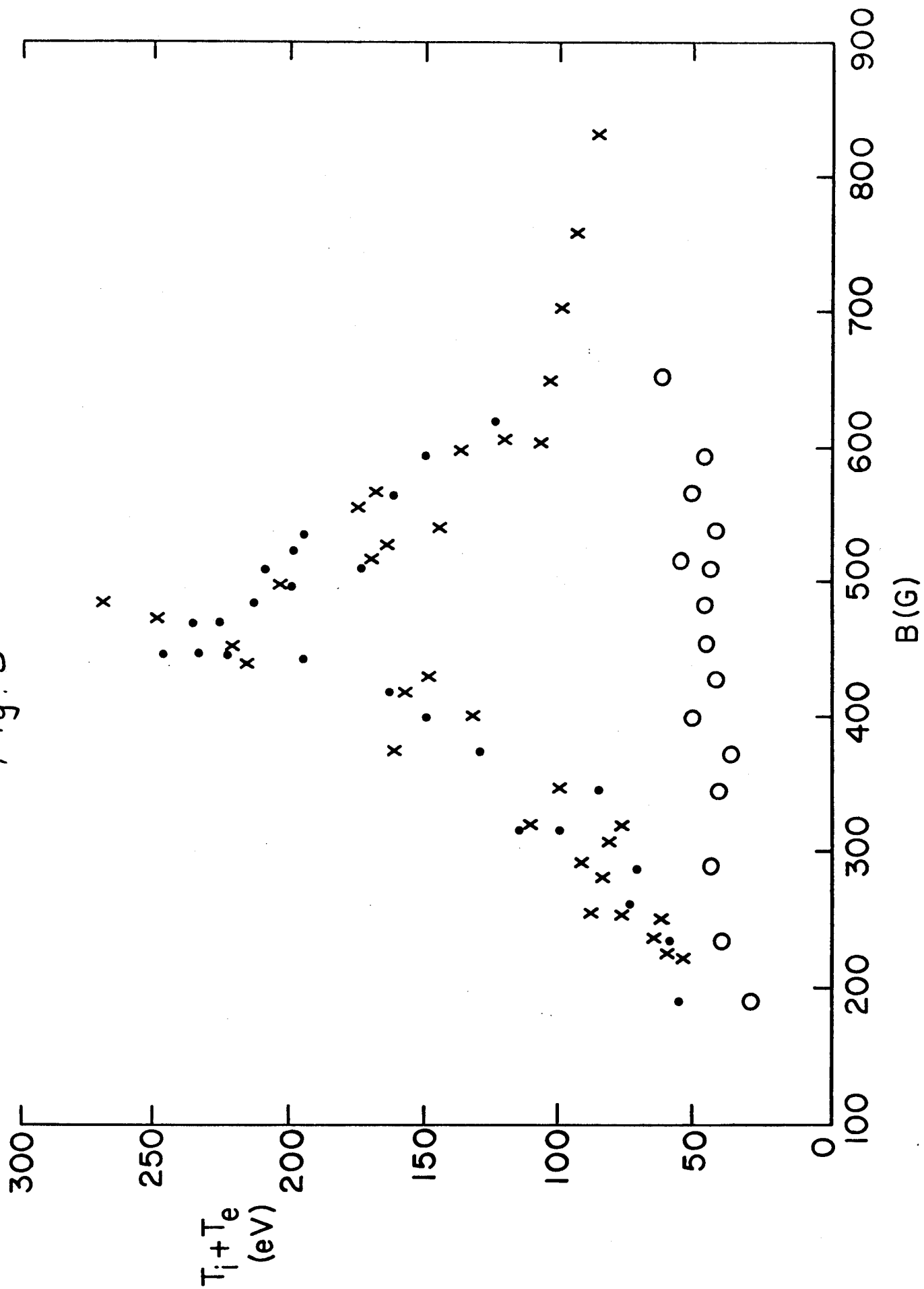


Fig. 9

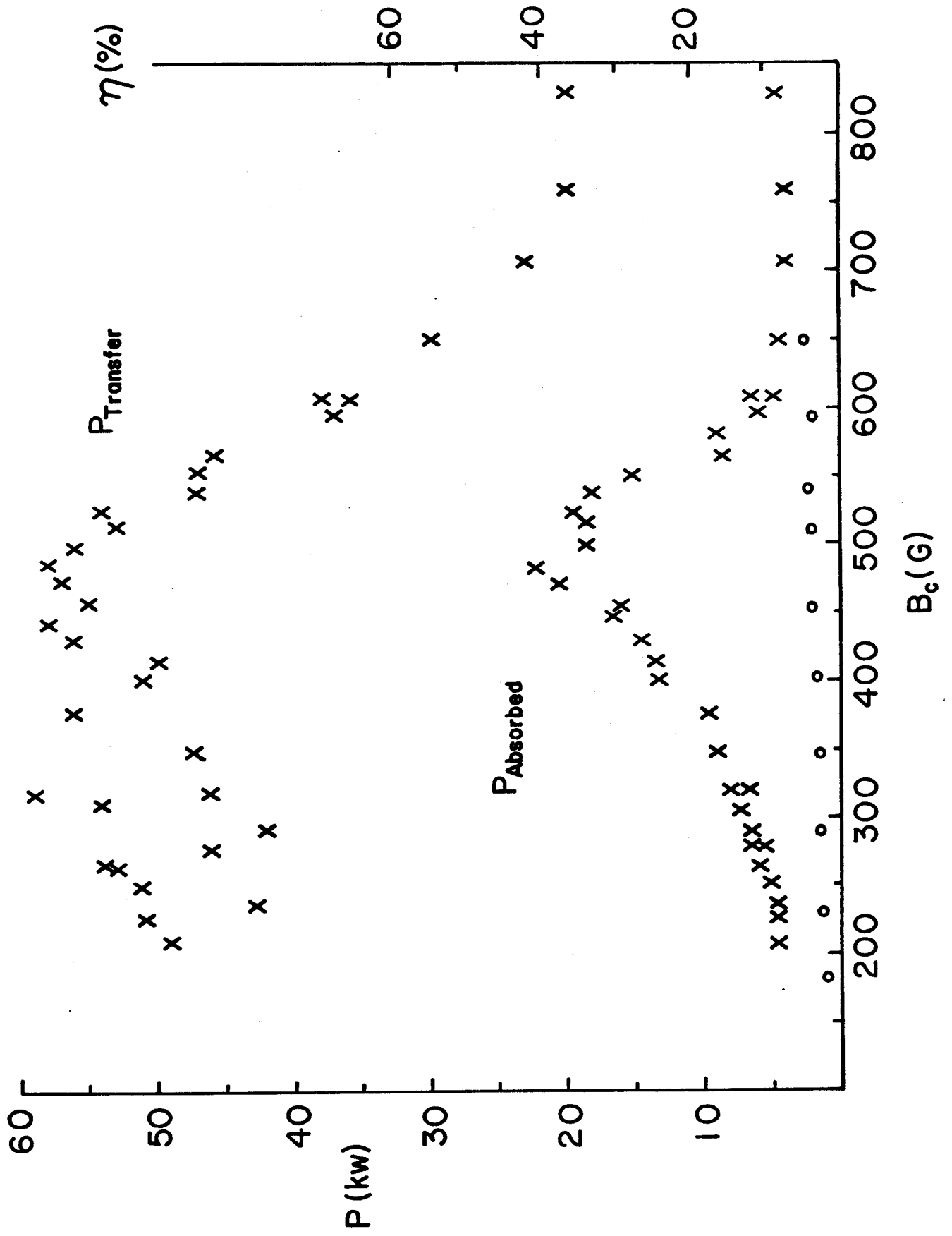
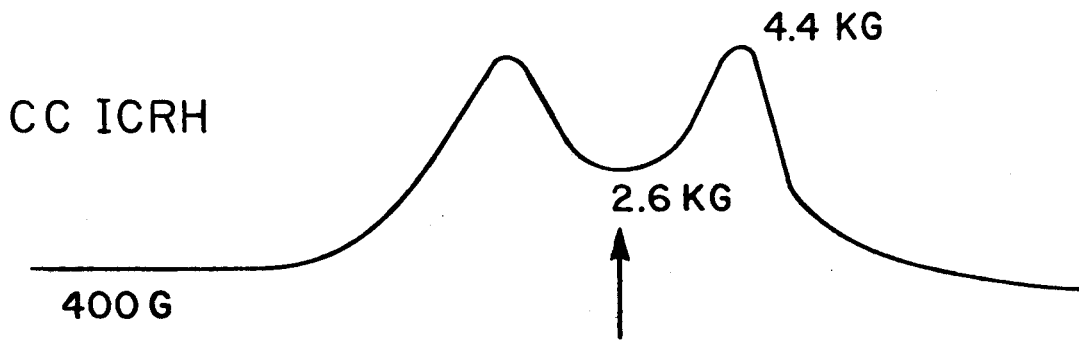


Fig. 10



Thomson Scattering

@ 1.4 ms

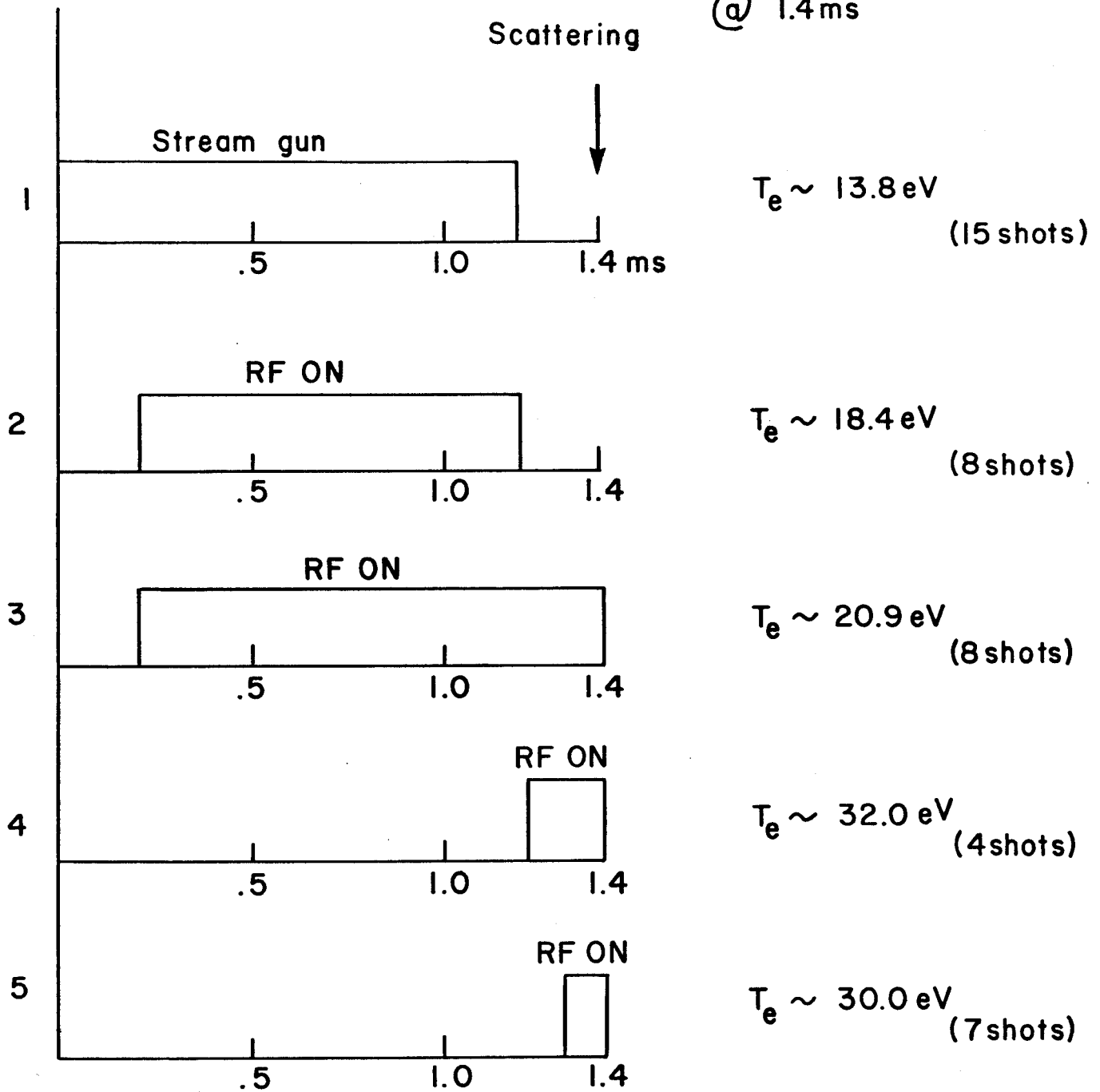


Fig. 11

→ $\Gamma_{H_2} = \frac{n_0(H_2)V_0}{2}$

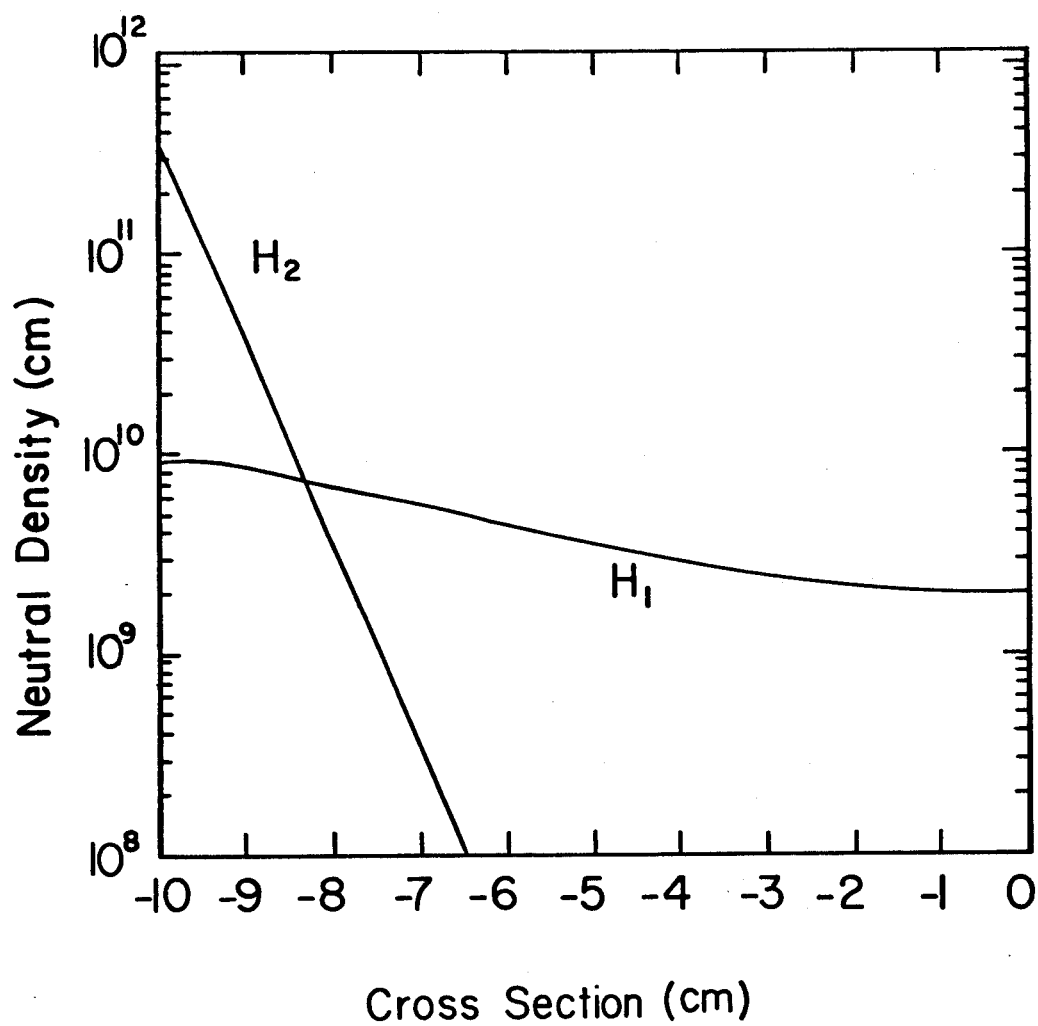


Fig. 12

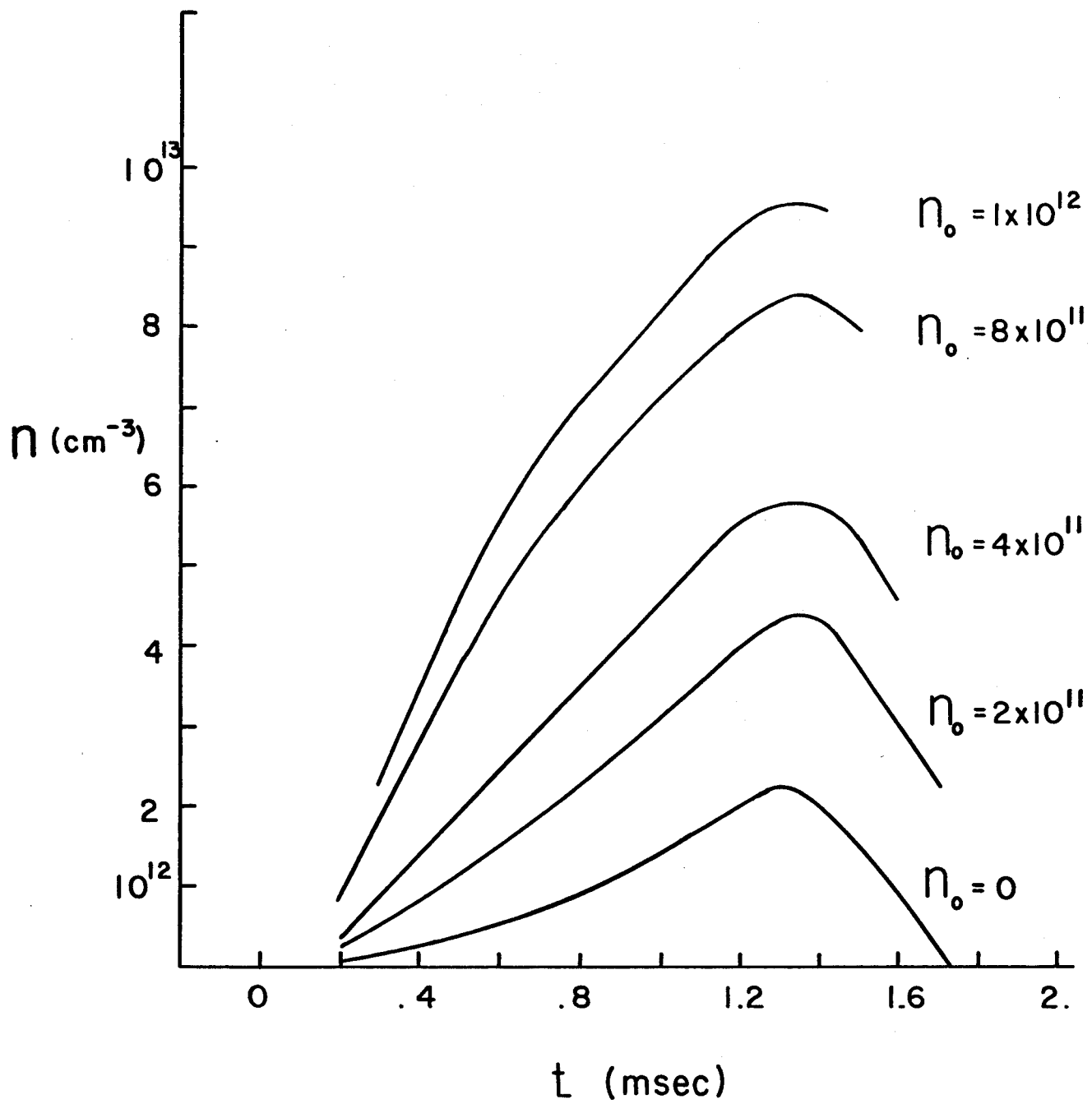


Fig. 13

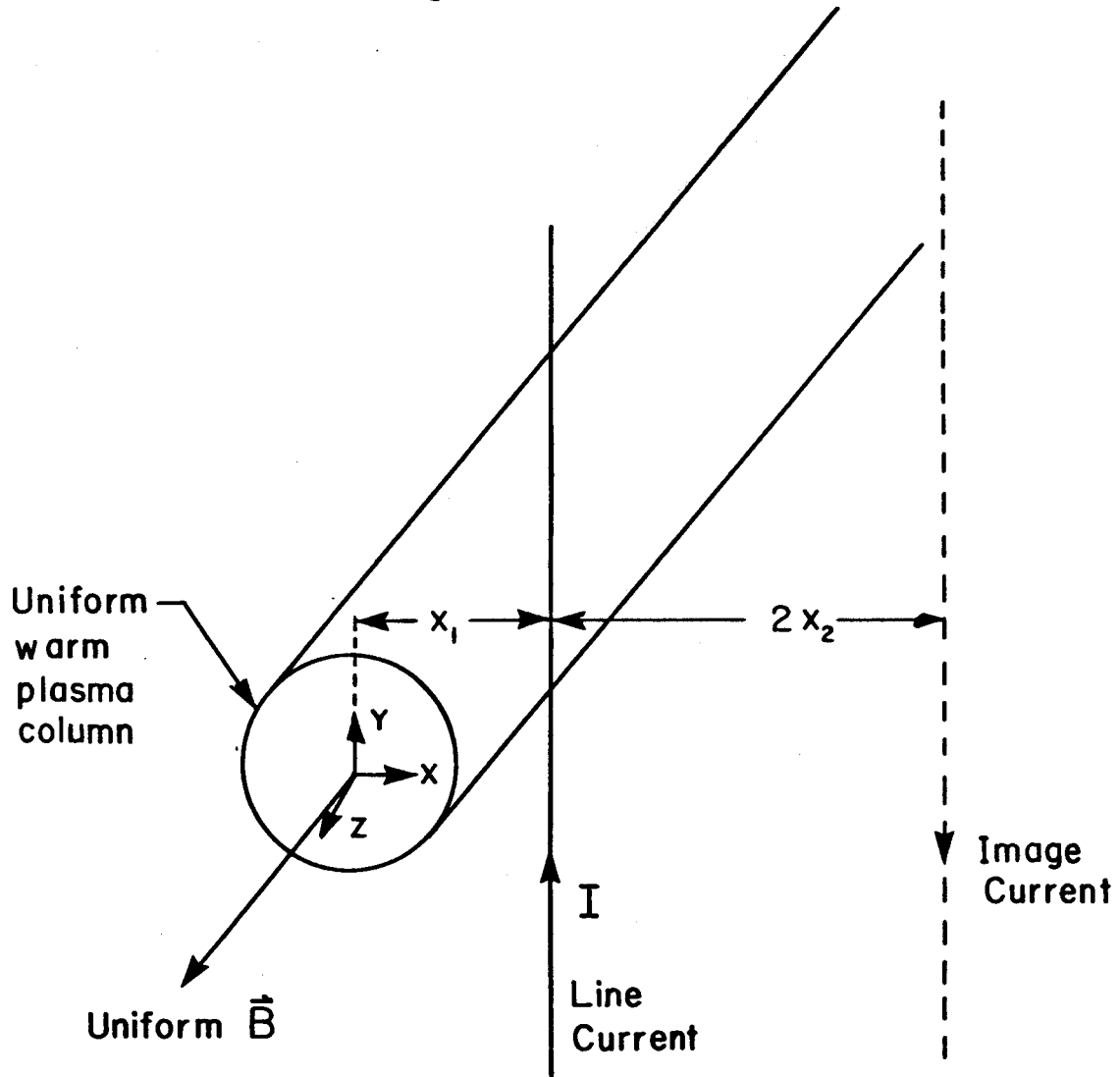


Fig. 14

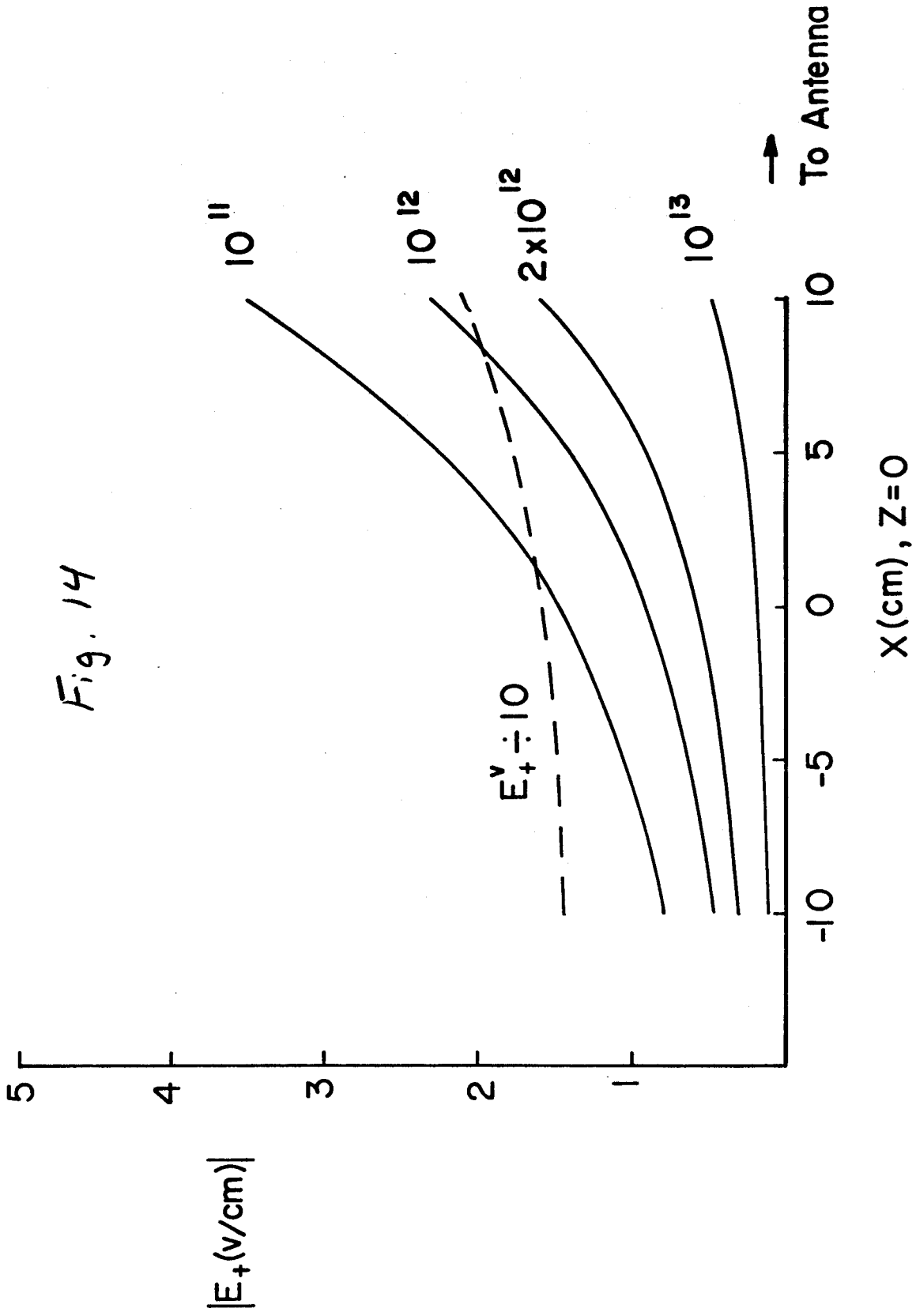
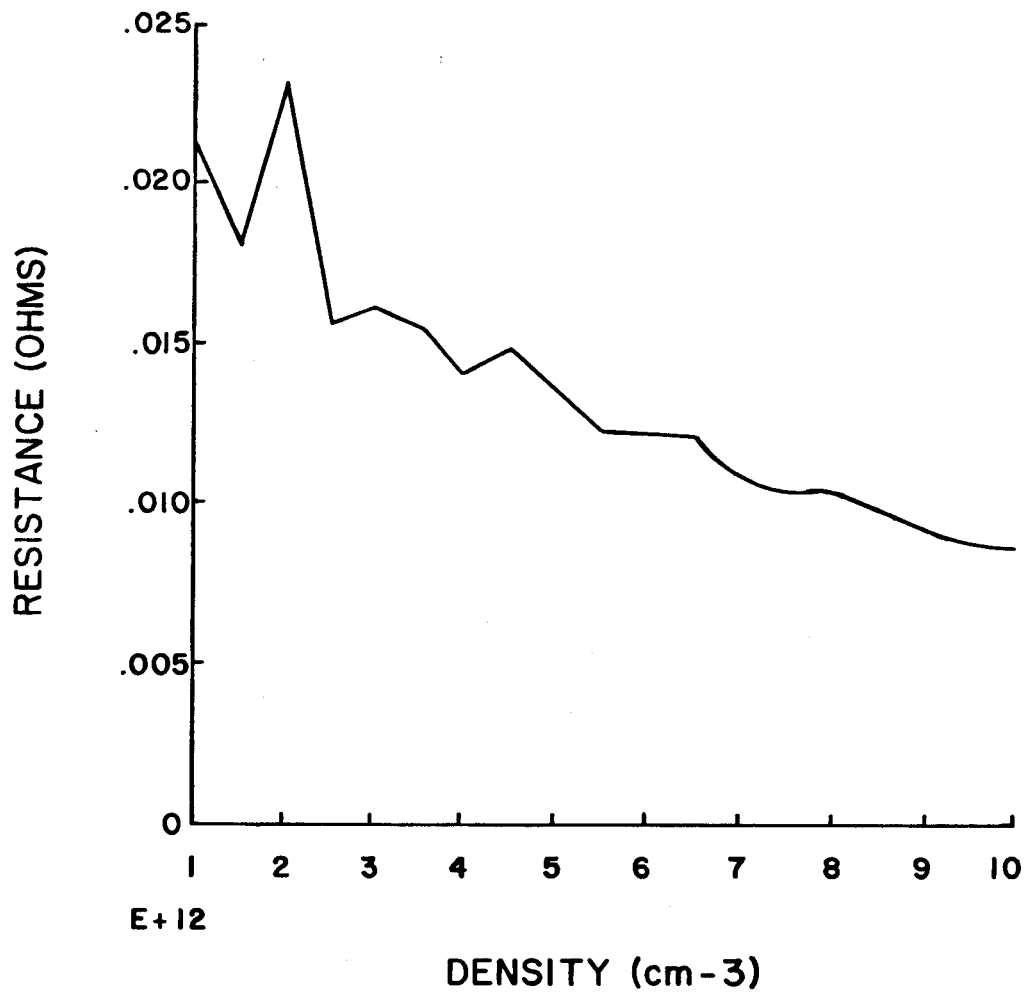


Fig. 15



P_{MAX}(W) = 4.60E + 4